Engineering Applications of Computational Fluid Mechanics Vol. 6, No.1, pp. 110–122 (2012)

NUMERICAL SIMULATION OF AIRFLOW AND PARTICLE COLLECTION BY VEGETATIVE BARRIERS

Li Guo and Ronaldo G. Maghirang *

Department of Biological and Agricultural Engineering, Kansas State University, Manhattan, KS 66506-5205 U.S.A.
** E-Mail: rmaghir@ksu.edu (Corresponding Author)*

ABSTRACT: Vegetative barriers have the potential to mitigate particulate matter (PM) from open dust sources, including unpaved and paved roads, exposed storage piles, and agricultural sources; however, data on their effectiveness in capturing PM are limited. This study was conducted to predict the airflow and particle collection efficiency of vegetative barriers. The applicability of computational fluid dynamics (CFD) in modeling airflow around and through porous barriers was first evaluated by simulating airflow passing a porous fence (1.2 m high × 0.01 m thick, 50% porosity) using standard and realizable k -ε turbulence models in FLUENT. Predicted air velocities compared favorably with available experimental data. The CFD model was then applied to simulate airflow and particle collection by a row of trees (2.2 m high × 1.6 m wide) with characteristics similar to those of hawthorn trees. The Eulerian-Eulerian model was used to predict particle transport and collection by the tree elements. Predicted particle collection efficiencies for the trees agreed with available experimental data and ranged from less than 1% for 0.875-μm particles to approximately 32% for 15-μm particles. Results from this study indicated that numerical simulation with CFD can be used to predict particle collection efficiency of vegetative barriers and that this technique has the potential to advance research on vegetative barriers for dust control for open sources. Further work is investigating effects of the structure of vegetative barriers on particle collection.

Keywords: computational fluid dynamics (CFD), fugitive dust, dust control, vegetative barriers

---

1. INTRODUCTION

Emissions of particulate matter (PM) are an increasing concern for open dust sources, including unpaved and paved roads, exposed storage piles, agricultural tilling, and animal feeding operations. Particulate matter generated from open sources has potential to reduce visibility and cause health problems in humans and livestock (Rogge et al., 2006; Purdy et al., 2004). Cost-effective abatement measures for mitigating PM emissions from open dust sources are needed.

Abatement measures for open dust sources generally fall into two major categories. The first is source control, which involves reducing emission rate through techniques such as removal of dust source material, watering of surfaces, and surface treatments. The second involves downwind control techniques, including vegetative barriers or porous fences to remove and/or disperse particles.

Field tests and wind tunnel experiments have been conducted to investigate the effects of natural and/or artificial windbreaks on airflow (Packwood, 2000; Wang and Takle, 1995; Wilson, 1985). Computational fluid dynamics (CFD) technique has also been applied in studying airflow due to natural and/or artificial windbreaks (Bitog et al., 2009; Tiwary et al., 2005; Packwood, 2000). Considerable progress in understanding airflow and turbulence characteristics has been achieved; however, the complexity of external and internal structures of vegetative barriers makes fully understanding their aerodynamics difficult (Lin, 2006). Besides the influence of vegetative barriers on airflow, vegetative barriers also affect particle concentration. Some of the oncoming particle-laden airflow passes over the barriers whereas some flows through, with particles filtered from the flow by deposition onto vegetation elements (leaves, trunks, or twigs) (Petroff et al., 2008a; Raupach et al., 2001). Currently, however, data on the effectiveness of vegetative barriers in removing or dispersing PM emitted from open dust sources are limited.

Clearly, research is needed to establish the efficiency of vegetative barriers in removing particles emitted from open sources. Field investigations into particle collection by vegetative barriers in open sources, however, are time-consuming and expensive. Particle dispersion simulation can be used to augment field investigations. However, more work is

---

Received: 2 Jul. 2011; Revised: 14 Oct. 2011; Accepted: 18 Oct. 2011

needed to determine a suitable resistance model and through-flow particle deposition process for a given geometry of windbreaks. In addition, selecting computationally efficient and accurate models for the simulation of particle-laden air flow is essential to obtain the airflow pattern and spatial distribution of particle concentration. The two commonly used approaches for modeling airflow and particle transport are Eulerian-Lagrangian and Eulerian-Eulerian. Many discussions on the relative advantages of each approach as they relate to the nature of the flow physics and numerical capabilities exist in the literature (Balakin et al., 2010; Tong and Luke, 2010). In this study, the Eulerian-Eulerian approach was employed for the relative ease and computational speed.

This study was conducted to determine effects of vegetative barriers on airflow and particle concentration using CFD. Specific objectives were to simulate airflow through porous fences and trees and to predict the particle collection efficiency of trees.

2. NUMERICAL FORMULATION

This research had two major components. The first component involved numerical simulation of airflow through a porous fence using CFD and comparing predicted results with available experimental data. The second component involved application of the CFD model to predict airflow and particle collection by a row of trees.

The CFD simulation process has three stages: pre-processing, solving, and post-processing (Tu et al., 2008). Gambit (ver. 2.3, Lebanon, NH, FLUENT, Inc.) was employed during pre-processing to develop the geometry of flow domain. FLUENT (ver. 6.3, FLUENT, Inc., Lebanon, NH) was used as the main module to perform CFD calculations. Post-processing, which involves organization and interpretation of predicted results, involved use of Excel (Microsoft Corporation, Redmond, WA) and Tecplot (ver. 360 2009, Tecplot, Inc., Bellevue, WA).

2.1 Simulation of airflow around a porous fence

In this study, a porous fence similar to that studied by Bradley and Mulhearn (1983) was considered. The fence was a vertical slat of wood (1.2 m × 0.01 m) with a porosity of 50%. To evaluate the applicability of the turbulence model, boundary conditions, porous barrier prediction, and predicted air velocities were compared with experimental data from Bradley and Mulhearn (1983).

2.1.1 *Computational domain*

A 2D computational domain (Fig. 1a) was used for the simulation. The discrete values of the flow properties such as air velocity and particle concentration were determined and described in each of these cells (Tu et al., 2008).

The grids were generated using straight edges. The origin of the horizontal axis (x = 0) was defined to lie at the location of the fence. For convenience, computational domains were denoted as where H and W are barrier height and width (Table 1), respectively; X_{up} is horizontal distance from the airflow inlet to the upwind edge of the barrier; X_{down} is horizontal distance from the origin to the airflow outlet; Z is distance from the ground to the upper boundary of the domain; R represents the stretching ratio from the barrier to outer boundaries for generating finer grids near the barrier region and coarser grids further away from the barrier region to reduce computational time and improve accuracy; and N_x and N_z denote numbers of cell columns and rows for the barriers (uniform vertical and horizontal spacing), respectively. The computational domain was set as $[-21,\ 125,\ 62,\ 0.01]_{1,\ 10}^{1.2}$ in accordance with Bourdin and Wilson (2008). The statistics of the computational grids are listed in Table 2. Fig. 1b shows the computational grids near the fence.

2.1.2 *Governing equations of continuous flow*

The 2D Reynolds-averaged Navier-Stokes (RANS) equations were the governing equations for the continuous flow field. Airflow was assumed to be steady, incompressible, and isothermal, and the neutrally stratified turbulent atmospheric surface layer was assumed.

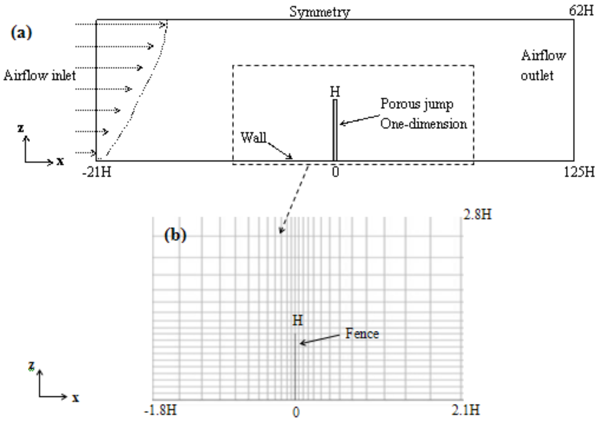

Fig. 1 Simulation of the porous fence: (a) geometry and domain (not drawn to scale; H is 1.2 m) and (b) computational grids near the fence.

Table 1 Input values for CFD models.

Parameter	Symbol	Value
Height of vegetative barrier (m)	H	1.2 (for fence) 2.2 (for tree)
Width of vegetative barrier (m)	W	0.01 (for fence) 1.6 (for tree)
Air density (kg/m^3)	ρ	1.225
Air dynamic viscosity (N·s/ m^2)	μ	1.79×10^{-5}
Air temperature (K)	T	293
Atmospheric pressure (Pa)	P	101325
Turbulence model constant	$C_{1\varepsilon}$	1.44
Turbulence model constant	$C_{2\varepsilon}$	1.92
Turbulence model constant	C_{μ}	0.09
Turbulent Prandtl number for k	σ_k	1.0
Turbulent Prandtl number for ε	σ_ε	1.3
von Karman constant	κ	0.4187
Particle density (kg/m^3)	ρ_p	1050
Mean free path (μm)	λ	0.066
Boltzmann constant (N·m/K)	ζ	1.38×10^{-23}
Turbulent Schmidt number	Sc_t	0.7
Polhausen coefficient	C_{Pol}	1.32

Table 2 Computational grids for porous fence and trees.

		Porous fence	Trees
Cells		2220	58000
Faces		4537	116722
Nodes		2318	58722
x coordinate (m)	min	-25.2	-66
	max	150	110
z coordinate (m)	min	0	0
	max	74.4	17.6
Volume (m^3)	min	6.4×10^{-3}	5.3×10^{-3}
	max	308	0.2
Face area (m^2)	min	6.0×10^{-2}	3.9×10^{-2}
	max	25	1.1

Equations for continuity and momentum conservation are as follows (Rosenfeld et al., 2010; Tu et al., 2008; FLUENT Inc., 2006):

$$\frac{\partial u_i}{\partial x_i}=0 \tag{1}$$

$$\rho u_j\frac{\partial u_i}{\partial x_j}=-\frac{\partial P}{\partial x_i}+\frac{\partial}{\partial x_j}\left(\mu\frac{\partial u_i}{\partial x_j}\right)+S_i \tag{2}$$

where x_i, x_j is Cartesian coordinate (m); u_i and u_j are velocity components (m/s) in the stream-wise and vertical directions, respectively; ρ is air density (kg/m^3); P is pressure (Pa); μ is air dynamic viscosity (N•s/m^2); and S_i is source term. S_i was assumed to be zero everywhere except for the porous barrier, which was treated as a momentum sink as discussed in Section 2.1.4. Values of ρ, P, and μ are listed in Table 1.

Standard and realizable k-ε models were used in this study based on previous studies (Rosenfeld et al., 2010; Bourdin and Wilson, 2008; Lin, 2006; Tiwary et al., 2005). The transport equations for the standard k-ε model (FLUENT Inc., 2006) are as follows:

$$\frac{\partial}{\partial x_i}\left(\rho k u_i\right)=\frac{\partial}{\partial x_j}\left[\left(\mu+\frac{\mu_t}{\sigma_k}\right)\frac{\partial k}{\partial x_j}\right] +G_k+G_b-\rho\varepsilon-Y_M \tag{3}$$

$$\frac{\partial}{\partial x_i}\left(\rho \varepsilon u_i\right)=\frac{\partial}{\partial x_j}\left[\left(\mu+\frac{\mu_t}{\sigma_\varepsilon}\right)\frac{\partial \varepsilon}{\partial x_j}\right] +C_{1\varepsilon}\frac{\varepsilon}{k}\left(G_k+C_{3\varepsilon}G_b\right)-C_{2\varepsilon}\rho\frac{\varepsilon^2}{k} \tag{4}$$

where G_k represents generation of k due to mean velocity gradients, calculated as $G_k=-\rho\overline{u_i' u_j'}\frac{\partial u_j}{\partial x_i}$;

G_b is generation of k due to buoyancy, calculated as $G_b = \beta g_i \frac{u_t}{Pr_t}\frac{\partial T}{\partial x_i}$; Pr_t is turbulent Prandtl number for energy and equal to 0.85; g_i is component of the gravitational vector in the i^{th} direction; and β is coefficient of thermal expansion and is defined as $\beta = -\frac{1}{\rho}\left(\frac{\partial \rho}{\partial T}\right)_P$. In Equation 3, Y_M represents the contribution of the fluctuating dilatation in compressible turbulence to the overall dissipation rate; $C_{1\varepsilon}$ and $C_{2\varepsilon}$ in Equation 4 are constants (Table 1); $C_{3\varepsilon}$ in Equation 4 is constant calculated as $C_{3\varepsilon} = \tanh|v/u|$, in which $C_{3\varepsilon}$ =1 for buoyant shear layers that main flow direction is aligned with the direction of gravity and $C_{3\varepsilon}$ =0 for buoyant shear layers that are perpendicular to the gravitational vector; and σ_k and σ_ε are turbulent Prandtl numbers for k and ε, respectively (Table 1). The Boussinesq hypothesis is employed to relate Reynolds stresses to mean velocity gradients. The turbulent (or eddy) viscosity, μ_t, is computed by combining k and ε as $\mu_t = \rho C_\mu \frac{k^2}{\varepsilon}$, where C_μ= 0.09.

The realizable *k-ε* model differs from the standard *k-ε* model in two ways (FLUENT Inc., 2006): (1) it has a new formulation for turbulent viscosity, and (2) the transport equation for ε is based on an exact equation for the transport of the mean-square velocity fluctuation. The expression for normal Reynolds stress in an incompressible strained mean flow is obtained by combining the Boussinesq relationship and the eddy viscosity definition as $\overline{u_i^2} = \frac{2}{3}k - 2\frac{\mu_t}{\rho}\frac{\partial U}{\partial x_i}$. To ensure realizability, i.e., positivity of normal stresses and Schwarz inequality for shear stresses ($\overline{u_i' u_j'} \le \overline{u_i'^2 u_j'^2}$), C_μ is sensitized to mean flow and turbulence (k,ε).

The pressure-based solver used the SIMPLE (Semi-Implicit Method for Pressure-Linked Equations) method to introduce pressure into continuity equation. The entire set of simulations was run using a second-order upwind scheme. For local residuals of continuity, momentum, turbulence, and scalars, the absolute criterion of convergence was set to 0.0001 over 1000 iterations. In most cases, from 500 to 700 iterations were needed to achieve convergence.

2.1.3 Boundary conditions

Boundary conditions in this study are shown in Fig. 1a (Bourdin and Wilson, 2008; Santiago et al., 2007; Wilson and Yee, 2003). At the upper boundary, a symmetry boundary condition was imposed. Outlet airflow was considered fully developed and was treated as outflow. No slip condition was used on the ground with roughness height, z_0 (m), which was set equal to 0.0017 H (Bourdin and Wilson, 2008). The standard wall function was applied for the near-wall treatment.

The inlet velocity profile used in the simulation corresponded to the logarithmic profile was (Bourdin and Wilson, 2008; Santiago et al., 2007):

$$u_{in} = \frac{u_*}{\kappa}\ln\left(\frac{z}{z_0}\right) \qquad (5)$$

$$v_{in} = 0$$

where u_{in} and v_{in} are inflow velocity at stream-wise and vertical directions (m/s), respectively; z is height from the ground (m); κ is von Karman constant; and u_* is friction velocity far upstream from the barrier. For the porous fence, u_* = 0.4 m/s (Bourdin and Wilson, 2008).

The magnitude of turbulent kinetic energy (k_{in}) and dissipation (ε_{in}) at the inlet can significantly influence the CFD solution. In the absence of measurement of k_{in} and ε_{in} in, the following equations (Bourdin and Wilson, 2008; Santiago et al., 2007) were used based on the assumption of equilibrium boundary layer:

$$k_{in} = \frac{u_*^2}{\sqrt{C_\mu}} \qquad (6)$$

$$\varepsilon_{in} = \frac{u_*^3}{\kappa z} \qquad (7)$$

2.1.4 Simulation of fence as momentum sink

Aerodynamically, porous barriers are wind momentum sinks (i.e., pressure loss) when the rough surface interacts with airflow above and within it. Momentum is absorbed from the flow by both form and skin-friction drags on elements and transported mainly by turbulent diffusion to produce the leeward wind speed reduction (Bourdin and Wilson, 2008; FLUENT Inc., 2006; Lin 2006; Tiwary et al., 2005).

Porous barriers can be treated as a pressure discontinuity surface by applying a porous medium condition (porous jump for fence or porous zone for tree). The porous medium may be normally modeled with a viscous loss term (I) and inertial loss term (II), as shown in Equation 8 (FLUENT Inc., 2006). The model was added to the standard fluid flow equation as a momentum sink.

$$S_i = -\Big(\underbrace{\frac{\mu}{\alpha} u_i}_{\text{I}} + \underbrace{C_2 \frac{1}{2} \rho |u| u_i}_{\text{II}}\Big) \tag{8}$$

where α is permeability (m^2), C_2 is inertial resistance (m^{-1}), and S_i is equivalent to pressure gradient and the pressure drop is related to the porosity of the medium.

The porous jump condition is a one-dimensional simplification of the porous medium model (FLUENT Inc., 2006). For turbulent flow and modeling of a perforated plate, the viscous loss term can be ignored (Bourdin and Wilson, 2008; FLUENT Inc., 2006). Consequently, the face permeability in the user inputs for the porous jump model in FLUENT was set as $1e^{+20}$ m^2. C_2 is related to the resistance coefficient or pressure loss coefficient (k_r) of the porous barrier and can be expressed as (Bourdin and Wilson, 2008; Wilson, 1985; FLUENT Inc., 2006; Tiwary et al., 2005):

$$C_2 = \frac{k_r}{W} \tag{9}$$

where k_r is dynamic parameter that depends on porosity and shape of the barrier elements (Wang and Takle, 1995). For the porous fence, k_r = 4 (Wilson, 1985; Bourdin and Wilson, 2008; Santiago et al., 2007). With W = 0.01 m, the pressure-jump coefficient, C_2 = 400. Inputs for porous jump models in FLUENT are summarized in Table 3.

Table 3 User inputs for porous medium models in FLUENT.

	Porous fence	Tree
Model	Porous jump	Porous zone
User inputs in FLUENT	Face permeability (m^2)=$1e^{+20}$	Direction-1 vector: X=0, Y=1
	Porous medium thickness (m)=0.01	Inertial resistance: Direction-1 (m^{-1})=0 Direction-2 (m^{-1})= $C_d d_{SA}$ (using UDF)
	Pressure-jump coefficient (m^{-1}) =400	Power law model: C_0=0, C_1=0 Fluid porosity: Porosity=1 (all fluid)

2.2 Simulation of airflow and particle transport for trees

The airflow around and through a row of trees was simulated considering their external and internal structures. An Eulerian-based model of particle transport through a tree was explored in this study, in which the number concentrations of different-sized particles were calculated using a modified User-Defined Scalars (UDS) equation by implementing User-Defined Functions (UDFs) in FLUENT. Fluid flow was first solved without considering the presence of particles, and then particle flow was calculated based on the solution of fluid flow (Wang and Lin, 2006).

2.2.1 Computational domain

Computational domain size and geometry of the row of trees (Fig. 2a) were based on research on hawthorn trees by Tiwary et al. (2005). The origin of the horizontal axis (x = 0) was defined to lie at the downwind edge of the tree. The computational domain was set as $[-30,\ 50,\ 8,\ 1.6]^{1.01}_{10,\ 16}$. The length of the edge of each cell within the tree was in x direction and in y direction. The statistics of the computational grids are listed in Table 2. Fig. 2b shows the grid pattern near and within the tree.

2.2.2 Governing equations and numerical solver

The governing equations for airflow and assumptions were similar to those for the porous fence. Equations 1 and 2 were also used for continuity and momentum conservation. The source term S_i in Equation 2 was assumed to be zero everywhere except the tree, which was treated as a momentum sink. Standard and realizable k-ε models were also used. For local residuals of continuity, momentum, turbulence and scalars, the absolute criterion of convergence was set to 0.0001 over 1000 iterations. In most cases, from 600 to 1300 iterations were needed to achieve convergence.

2.2.3 Boundary conditions

Boundary conditions for the trees are shown in Fig. 2a (Tu et al., 2008; Tiwary et al., 2005; Packwood, 2000). Similar to the fence, a symmetry boundary condition was imposed at the upper boundary and outlet airflow was treated as outflow. No slip condition was used on the ground with roughness height z_0 = 0.0086 H based on the studies of Tiwary et al. (2005) and Packwood (2000). The inlet velocity profile used in the simulation corresponded to the logarithmic

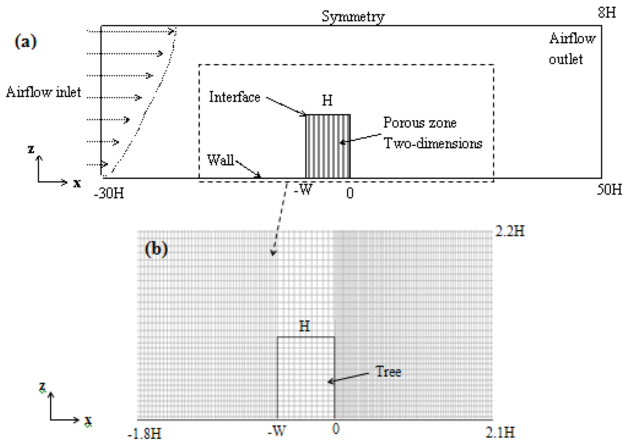

Fig. 2 Simulation of the trees: (a) geometry and domain (not drawn to scale; H is 2.2 m) and (b) computational grids near the tree.

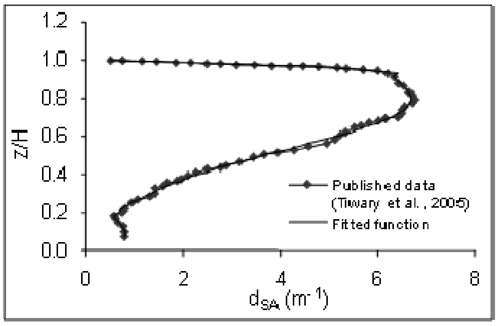

Fig. 3 Surface area density (d_{SA}) for trees as a function of height (H is 2.2 m) (Tiwary et al., 2005).

profile as in Equation 5, in which $u_* = 0.0548\ U_{OH}$. U_{OH} was air velocity at x/H = -10 and z/H = 1. A value of 2.3 m/s was used for U_{OH} based on available experimental data (Tiwary et al., 2005). Equations 6 and 7 were also used for the magnitudes of turbulent kinetic energy (k) and dissipation (ε_{in}) at the inlet.

2.2.4 Simulation of trees as momentum sink

The row of trees was treated as a porous zone and was simulated based on Equations 8 and 9 (Tiwary et al., 2005; FLUENT Inc., 2006; Wilson, 1985). For ambient airflow, viscous loss term in Equation 8 was ignored (Tiwary et al., 2005). Thus, viscous resistance in the user inputs of FLUENT for the porous zone model was set as 0. The k_r, related to C_2, was the product of local leaf area density d_{SA} (m^{-1}) and drag coefficient C_d (normal range of 0.1 to 0.5) (Rosenfeld et al., 2010; Melese Endalew et al., 2009; Tiwary et al., 2005; Wilson, 1985). Consequently, the inertial resistance at the z-direction was set as $C_2 = C_d d_{SA}$. The d_{SA} values were extracted from Tiwary et al. (2005) and fitted into functions related to heights from the ground as shown in Fig. 3. Inputs for the porous zone model in FLUENT are summarized in Table 3.

2.2.5 Particle transport

Processes of particle deposition onto vegetative barriers include transport of particles by turbulence and sedimentation and collection by the different elements of the barriers, including stems, twigs, and leaves. Particle collection by these elements combines the collection efficiency due to diffusion, impaction, and interception, whereas other processes such as thermophoresis or electrophoresis were neglected because they are less important for natural plant surfaces (Petroff et al., 2008a). The overall collection efficiency of a single element is equivalent to the sum of the components.

The particle-laden airflow was treated as a two-phase mixture of air and particles. The Eulerian-Eulerian approach was used because of its computational efficiency and relative ease of integration into Eulerian-based CFD codes. In this approach, both phases were considered as two continua and treated mathematically by solving conservation equations for both phases. Similar to previous studies (Tong and Luke, 2010; Zhang et al., 2008; Portela and Oliemans, 2006), one-way coupling was assumed for relatively low particle concentration without considering the collision of particles. Spherical particles with density of 1050 kg/m^3 and diameters (d_p) of 0.875, 1.5, 2.75, 4.25, 6.25, 8.75, 12.5, and 15 μm, based on Tiwary et al. (2005), were considered in this study.

The particle number concentration (N) was solved by a modified scalar transport equation coupled with the flow field as (Zhang et al., 2008; FLUENT Inc., 2006; Hinds, 1999):

$$\frac{\partial(u_i N_k)}{\partial x_i} - \frac{\partial}{\partial x_i}\left(\Gamma_k \frac{\partial N_k}{\partial x_i}\right) = -U_{sk}\frac{\partial N_k}{\partial x_i} + S_k \qquad k = 1, 2, ..., 8 \tag{10}$$

where N_k is number concentration of the kth group of particles with known diameter d_p (i.e., 0.875, 1.5, 2.75, 4.25, 6.25, 8.75, 12.5, and 15 μm); Γ_k is diffusivity coefficient of particles in air; and U_{sk} is particle settling speed of the kth group of particles, defined as $U_{sk} = C_c \tau_p g$, where C_c is slip correction factor defined as

$C_c = 1 + \frac{\lambda}{d_p}\left[2.34 + 1.05\exp\left(-\frac{0.39d_p}{\lambda}\right)\right]$, λ is the mean free path (μm), g is gravitational acceleration (m/s^2), and τ_p is particle relaxation time defined as $\tau_p = \frac{\rho_p d_p^2}{18\mu}$. A uniform profile of particle concentration was assumed at the inlet of the domain, in which an arbitrary value N_0 was applied.

In Equation 10, Γ_k combines the laminar and turbulent diffusion components, Γ_D and Γ_T ($\Gamma_k = \Gamma_D + \Gamma_T$).The laminar diffusion coefficient, Γ_D, is calculated using the Stokes-Einstein equation as

$$\Gamma_D = \frac{\zeta T C_c}{3\pi\mu d_p} \tag{11}$$

where ζ is Boltzmann constant, T is absolute temperature (K), and μ is dynamic viscosity of the air. The turbulent diffusion coefficient, Γ_T, is defined as

$$\Gamma_T = \frac{\nu_t}{Sc_t} \tag{12}$$

where ν_t is turbulent viscosity and Sc_t is turbulent Schmidt number. The turbulent Schmidt number is a measure of the relative diffusion of momentum and mass due to turbulence. Because the Schmidt number is an empirical constant that is relatively insensitive to the molecular fluid properties, Sc_t was set to 0.7 for all cases (Table 1) (Zhang et al., 2008; Hinds, 1999).

In Equation 10, S_k is the source term. Outside the barriers, its value is zero. Inside the barriers, on the other hand, it represents particle flux change per volume. The total number of particles collected by the tree can be determined using (Tiwary et al., 2005):

$$F = \int_0^H \int_{-W}^0 u(x,z)(N_{in} - N_{out})dxdz \tag{13}$$

where $u(x,z)$ is face velocity profile of the grid cell, N_{in} is particle concentration entering a cell, and N_{out} is particle concentration emerging from the cell. The collection efficiency of the elements of the tree in each cell can be calculated as

$$CE_{cell} = \frac{N_{in} - N_{out}}{N_{in}} \tag{14}$$

Then, Equation 13 can be expressed as

$$F = \int_0^H \int_{-W}^0 u(x,z)CE_{cell}N_{in}dxdz \tag{15}$$

Consequently, the source term can be calculated as Equation 16 considering only the horizontal wind advection, i.e.,

$$S_k = -\frac{uCE_{cell}N_{in}\Delta z}{V} \tag{16}$$

where V is cell volume. CE_{cell} was estimated by accounting for the different collection mechanisms of the tree elements in each grid cell as described in Section 2.2.6.

2.2.6 Calculation of particle collection efficiency of vegetation elements

Tree elements such as leaves, stems, and twigs can be treated as filter fibers that interact with and collect particles. Specific geometrical properties (i.e., shape, size, and orientation) of each element contribute to collection; however, models do not reflect this variability, and an implicit averaging operation over the elements has been applied in most cases (Petroff et al., 2008a).

Two main particle collection mechanisms were considered in this study: Brownian diffusion and inertial impaction (Tiwary et al., 2005; Raupach et al., 2001; Hinds, 1999). Brownian diffusion is the dominant collection mechanism for very fine particles (Hinds, 1999; Petroff et al., 2008a). It is modeled through the theory of particle diffusion over smooth infinite cylinders perpendicular to the flow. The boundary layer state (laminar or turbulent) of individual elements depends on the Reynolds number built upon the element characteristic size and the average flow velocity, and affects transfer by diffusion (Petroff et al., 2008b).The single element efficiency due to diffusion, ED, is (Raupach et al., 2001)

$$E_D = \frac{\Gamma_D C_{Pol} \mathrm{Re}^{\frac{1}{2}} Sc^{\frac{1}{3}}}{d_e U_{cell}} \tag{17}$$

where C_{pol} is the Polhausen coefficient equal to 1.32 for a two-sided flat plate; d_e is diameter of the element with an average of 6 mm ranging from 2 mm to 10 mm (Tiwary et al., 2005); U_{cell} is air velocity in each cell; Sc is Schmidt number, given by $Sc = \frac{\mu}{\Gamma_D \rho}$; and Re is Reynolds number for flow around an element of cross-section d_e, defined as $Re = \frac{\rho d_e U_{cell}}{\mu}$.

Inertial impaction occurs when a particle with large inertia is unable to adjust quickly to follow the streamline and collides with the tree elements (Petroff et al., 2008a; Hinds, 1999). Single element collection efficiency (E_I) due to inertial impaction is commonly expressed as (Tiwary et al., 2005; Raupach et al., 2001):

$$E_I = \left(\frac{St}{St + 0.8} \right)^2 \tag{18}$$

where St is Stokes number and is defined as $St = \frac{d_P{}^2 \rho_P U_{cell}}{18 \mu d_e}$.

Collection via diffusion should be estimated for each element type by using the d_{SA} and via impaction by using only the projected surface area, which is related to the angle (θ) between the element orientation and stream-wise direction. The collection mechanism for leaves is different from that of other elements such as stems, because the orientation of leaves may be changed by the wind (Wilson and Yee, 2003); however, the angle variation of those elements was not considered in this study. Instead, a weighting factor r of 1.9 assuming θ = 90° (Tiwary et al., 2005) was applied to calculate the overall collection efficiency of all tree elements. The overall collection efficiency contributed by the tree within each grid cell was expressed as

$$CE_{cell} = r \left[1 - \exp\left(-d_{SA} (E_I + E_D) \Delta x \right) \right] \tag{19}$$

and particle collection by the tree at certain height was calculated by

$$CE = \frac{N_{up} - N_{down}}{N_{up}} \tag{20}$$

where N_{up} and N_{down} are number concentrations at the upwind and downwind sides of the tree at that height, respectively.

2.3 Data analysis

Previous research indicated that vegetative barriers can provide shelter for some distance downwind and their efficiency may be determined by how wind speed and turbulent flow are modified (Raupach et al., 2001; Cleugh, 1998). Cleugh (1998) indicated that the effectiveness of a porous barrier as shelter can be quantified according to the following parameters:

1. ratio of wind speed (normalized velocity) measured near the barrier (u) to a reference wind speed (u_0) that is not affected by the barrier;
2. minimum downwind speed (u_{min}) and downwind distance (x_{min}) to u_{min}; and
3. distance (x_s) to $u/u_0 < c$, where c is an arbitrary factor and is often 0.7 or 0.8.

Based on published experimental data (Bradley and Mulhearn, 1983), the upwind mean velocity at z =3.33 H was chosen as the reference velocity (u_0) for both the fence and tree. Normalized predicted velocities, u/u_0, at z =0.38 H and z =1.88 H were analyzed and compared with experimental data.

The sensitivity of predicted velocity to values of C_d and z_0 were assessed along with turbulent models. Normally, C_d ranges from 0.1 to 0.5 and 0.5 were used in the Tiwary et al. study (2005). They applied $z_0/H = 0.0086$ based on the study of airflow through fences conducted by Packwood (2000). This study applied these values and also adjusted them to determine their effects on airflow.

For particle collection, simulation was based on field measurements of particle concentration taken upwind and downwind of the tree (Tiwary et al., 2005). In Tiwary et al. (2005) study, two identical optical particle counters (OPCs) were placed at points of (x = -W – 0.1 H, z = 0.75 H) and (x = 0.1 H, z = 0.75 H) away from the tree. Predicted particle collection efficiencies (CEs) of the tree, which were calculated based on predicted concentration values at these two points, were compared with published experimental data using paired t-tests.

3. RESULTS AND DISCUSSION

3.1 Airflow around the porous fence

A roughly triangular-shaped wind speed reduction zone was formed and extended to far downwind of the fence as shown in the contours of normalized velocities (u/u_0) in Fig. 4a. A smaller portion of the wind speed reduction area was also observed on the windward side of the fence. Horizontal velocities above the fence increased sharply upward and showed slight decrease toward the ground, which is related to the displaced profile and mixing zone, respectively, in Fig. 4a. These results agreed with the observations described by Judd et al. (1996), in which the flow is divided into six distinct zones (approach profile, displaced profile, bleed flow, quiet zone, mixing zone, and re-equilibration zone). No recirculation region was evident, which

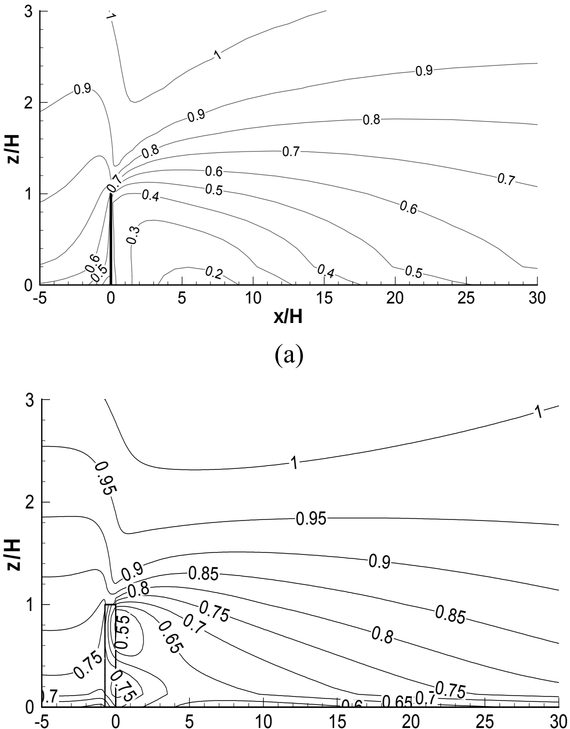

(a)

(b)

Fig. 4 Contours of normalized horizontal velocities (u/u_0): (a) for fence as predicted by the realizable k-ε model (H is 1.2 m), and (b) for tree predicted by realizable k-ε model with C_d = 0.16, z_0/H = 0.0086 (H is 2.2 m).

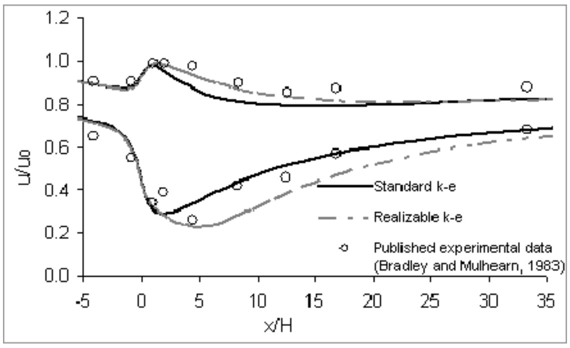

Fig. 5 Comparison of normalized predicted and experimental (Bradley and Mulhearn, 1983) air velocities for the porous fence at z = 0.38 H and z = 1.88 H (H is 1.2 m).

is consistent with the observation by Wang and Takle (1995) and Bradley and Mulhearn (1983), who found no evidence of a recirculating region when the porosity reached or exceeded 50%.

The normalized velocities (u/u_0) at z = 0.38 H and z = 1.88 H are shown in Fig. 5 along with experimental data from Bradley and Mulhearn (1983). In general, predicted normalized velocities for the two turbulence models agreed favorably with available experimental data. The standard k-ε model had better results at z = 0.38 H further downstream from the fence compared with the realizable k-ε model; however, at z = 1.88 H, the realizable k-ε model had better results. The slight difference in compatibility between predicted results and experimental data for different values of z may be due to the inherent characteristics of the turbulence models (Bourdin and Wilson, 2008). The $u_{\min}$ ($u_{min}/u_0 \leq 0.2$) was in the area of 3 H $\leq x_{min} \leq$9 H and z <0.2 H, x_s was also greater than 30 H for $u/u_0 < 0.7$ as shown in Fig. 4a. For the standard k-ε model (not shown), the u_{min} ($u_{min}/u_0 \leq$0.2) was in the area of 2 H $\leq x_{min} \leq$ 5 H and z <0.2 H, x_s was greater than 30 H for u/u_0 <0.7. The realizable k-ε model predicted slightly lower velocity downwind of the fence and higher velocity over the fence compared with the standard k-ε model. However, differences in predicted results between the two turbulence models were not considerable and both showed overall good performance in predicting airflow.

3.2 Airflow around and particle collection by trees

Similar to the porous fence, a roughly triangular-shaped wind speed reduction zone downwind of the tree was observed as shown in the contours of u/u_0 around the tree in Fig. 4b; the area was less than that for the fence. Two speed reduction zones were evident, which was caused by the different resistance of the tree at different heights with low and/or no resistance at the bottom of the tree. One was located at around -5 H and close to the ground, similar to that for the fence. Another was located within the upper part and at the downwind edge of the tree where k_r was higher. Predicted u/u_0 values increased within the lower part of the tree where k_r was lower or zero. Above the tree, the horizontal velocities also increased upward and showed slight decrease toward the ground. No separating recirculation zone was observed.

As expected, the predicted CE values increased with increasing particle size similar to published experimental data (Tiwary et al., 2005) as shown in Fig. 6. With z_0/H =0.0086 and C_d =0.5, CE values predicted by the realizable k-ε model were closer to experimental data, especially for particles with diameter greater than 5 μm, compared with the standard k-ε model. However, both models underestimated CEs for large particles compared with experimental data. A strong correlation existed between predicted CE and experimental data (Pearson correlations were greater 0.9); however, the P (T<= t) values were less than 0.05, indicating significant differences

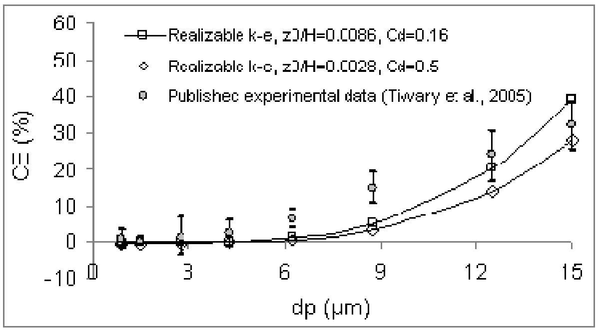

Fig. 6 Comparison of predicted and published experimental collection efficiencies (CEs) (Tiwary et al., 2005) for a row of trees. Predicted values were for the realizable k-ε model with C_d = 0.16, z0/H = 0.0086 and C_d = 0.5, z0/H = 0.0043 (H is 2.2 m).

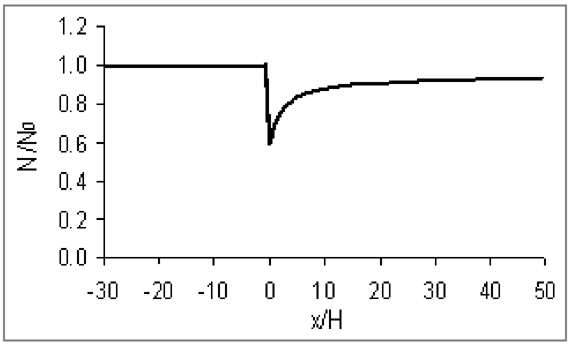

Fig. 7 Horizontal variation of normalized particle concentration (N/N_0) of d_p = 15 μm at z = 0.75 H predicted by realizable k-ε model with C_d = 0.16 and z0/H = 0.0086 (H is 2.2 m).

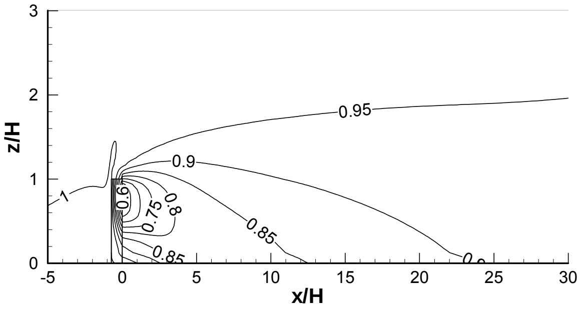

Fig. 8 Contours of normalized particle concentration (N/N_0) of d_p = 15 μm predicted by realizable k-ε model with C_d =0.16, z_0/H=0.0086 (H is 2.2 m).

between simulated and experimental values. Better agreements of predicted values and experimental data were observed when C_d = 0.16 (Fig. 6). Predicted CE values were within the range of experimental data, except particles with d_p = 6.25 μm and d_p = 8.75 μm, in which predicted values were smaller than experimental data. Paired t-tests did not show any significant difference between predicted values and experimental data. Adjusting z_0/H to 0.0028 did not improve the agreement between predicted values and experimental data (Fig. 6).

The horizontal variation of normalized particle concentration (N/N_0)) for d_p = 15 μm at z = 0.75 H predicted by the realizable k-ε model with C_d = 0.16 and z_0/H = 0.0086 was very slight at the upwind edge of the tree as shown in Fig.7. The concentration was reduced significantly through the tree and gradually increased far downwind of the tree. The near-surface particle concentration increased with increasing downwind distance from the tree because the flow above the tree was mixed downward into the sheltered region, eventually approaching the approximate values far upwind (Raupach et al., 2001; Judd et al., 1996). A closer look at the spatial distribution of predicted particle concentration with d_p = 15 μm, as shown in Fig. 8, indicated that particle concentration above the tree was slightly reduced, most likely due to the gravitational settling, and was greatly reduced near and within the tree. Higher reduction of concentration near the ground was observed at the stream-wise direction at a downwind distance of about 10 H. These indicate that particle collection efficiency of the tree may be improved by using taller trees and adding more rows of trees. Fig. 8 also shows the maximum reduction of particle concentration by the tree occurred at the upper part with high surface area density near the downwind edge of the tree, indicating that the surface area density and width of the trees have positive effects on the effectiveness of the tree.

Results from this study indicate that numerical simulation with CFD can be used to predict collection efficiency of vegetative barriers and that this technique has the potential to advance research on vegetative barriers for dust control for open sources. Further work is investigating the effects of the structure of vegetative barriers — geometry, species, number of rows — on particulate control efficiency. Such information will assist in optimally using vegetative barriers to reduce downwind concentrations.

4. CONCLUSIONS

This study investigated airflow around a porous fence using computational fluid dynamics (CFD). Predicted results agreed favorably with available experimental data. The CFD model was then applied to simulate airflow around and through a row of trees. In addition, an Eulerian-based model of particle transport was implemented in the CFD model to predict particle collection by the trees. Predicted particle collection efficiencies compared favorably with available experimental data.

In this study, the complexity of vegetative geometry was reduced empirically to a few parameters (such as surface area density, orientation, size and shape of individual element, and roughness length). In addition, physical and chemical interactions between particles and air were ignored. Even with these limitations, the study indicated the potential of numerical simulation with CFD to predict collection efficiency of vegetative barriers. Future work will focus on establishing effects of the structure of vegetative barriers — geometry, species, number of rows — on particle collection.

ACKNOWLEDGEMENT

This study was supported by the USDA-NIFA Special Research Grant "Air Quality: Reducing Air Emissions from Cattle Feedlots and Dairies (TX and KS)," through the Texas AgriLife Research and the Kansas Agricultural Experiment Station (contribution no. 11-375-J). The technical support of Dr. Zhongquan Zheng, Dr. Xiaofan Yang, Mr. Zhenglun Wei, and Dr. Ning Zhang are appreciated.

NOMENCLATURE

c	arbitrary factor to determine x_s
C_2	inertial resistance for porous medium model (m^{-1})
$C_{1\varepsilon}$,$C_{2\varepsilon}$,$C_{3\varepsilon}$	constants for $k-\varepsilon$ turbulence model
C_c	slip correction factor
C_d	drag coefficient
C_{pol}	Polhausen coefficient
C_μ	factor in computing eddy viscosity
CE	particle collection efficiency of tree at certain height of barrier (%)
CE_{cell}	particle collection efficiency of the elements of the tree in each cell (%)
CFD	computational fluid dynamics
d_e	diameter of tree element (mm)
d_p	particle diameter (μm)
d_{SA}	surface area density of tree (m^{-1})
E_D	collection efficiency of individual element of porous barrier due to diffusion (%)
E_I	collection efficiency of individual element of porous barrier due to impaction (%)
F	number of particles collected by the barrier per unit time (#/s)
g_i	gravitational vector in ith direction (m/s^2)
G_b	generation of turbulence kinetic energy due to buoyancy ($kg/m{\cdot}s^3$)
G_k	generation of turbulence kinetic energy due to the mean velocity gradient ($kg/m{\cdot}s^3$)
H	height of barrier (m)
k	turbulent kinetic energy (m^2/s^2)
k_{in}	turbulent kinetic energy of inflow (m^2/s^2)
k_r	resistance coefficient or pressure loss coefficient
N_{in}, N_{out}	particle concentration entering and emerging a cell ($\#/m^3$)
N_k	number concentration of the k^{th} scalar or particles ($\#/m^3$)
N_{up}, N_{down}	number concentration upwind and downwind of the barrier at certain height of barrier ($\#/m^3$)
N_x, N_z	Number of cell columns and rows for the barriers (uniform vertical and horizontal spacing)
P	pressure (Pa)
PM	particulate matter
Pr_t	turbulent Prandtl number for energy
r	weighting factor for total particle collection efficiency
R	stretching ratio from the barrier to outer boundaries
Re	Reynolds number for flow around an element
RANS	Reynolds-averaged Navier-Stokes
S_i	source term in the i^{th} direction
S_k	source term that can be supplied by the user for each of the scalar equations
Sc	Schmidt number
Sc_t	turbulent Schmidt number
St	Stokes number
SIMPLE	semi-Implicit Method for Pressure-Linked Equations
T	absolute temperature, K
u, v	velocity components in x and y directions (m/s)
u_0	reference wind speed (m/s)
u_i, u_j	air velocity in the i^{th} and j^{th} direction (m/s)
u_{in}, v_{in}	inflow velocities in x and y directions (m/s)
u_{min}	minimum downwind speed (m/s)

u_*	friction velocity (m/s)
U_{cell}	air velocity in each cell (m/s)
U_{sk}	particle settling speed of the k^{th} particle (m/s)
UDF	user-defined function
UDS	user-defined scalar
V	volume of each grid cell (m^3)
W	width of barrier (m)
x, z	horizontal and vertical axes
x_i, x_j	cartesian coordinate (m)
x_{min}	downwind distance to $u_{\min}$ (m)
x_s	distance to u/u_0<c (m)
X_{down}	horizontal distance from origin to airflow outlet (m)
X_{up}	horizontal distance from airflow inlet to the upwind edge of the barrier (m)
Y_M	contribution of the fluctuating dilatation in compressible turbulence to the overall dissipation rate
z_0	roughness height (m)
Z	distance from ground to upper boundary of the domain (m)
Δx, Δz	length of edge of each grid cell in x and z directions (m)

Greek letters

α	permeability of barrier (m^2)
ε	turbulent dissipation rate (m^2/s^3)
ε_{in}	turbulent dissipation rate of inflow (m^2/s^3)
β	coefficient of thermal expansion
θ	angle between the element orientation and the stream wise direction (°)
κ	von Karman constant
ρ	air density (kg/m^3)
ρ_p	particle density (kg/m^3)
μ	air dynamic viscosity ($N \cdot s/m^2$)
μ_t	turbulent (or eddy) viscosity ($kg/m \cdot s$)
σ_ε	turbulent Prandtl number for ε
σ_k	turbulent Prandtl number for k
ζ	Boltzmann constant ($N \cdot m/K$)
λ	mean free path (μm)
τ_p	particle relaxation time (s)
Γ	diffusion coefficient
Γ_D	molecular diffusivity coefficient
Γ_k	total diffusivity coefficient
Γ_T	turbulent diffusivity coefficient
υ	kinematic viscosity (m^2/s)
υ_t	local kinematic viscosity (m^2/s)

REFERENCES

1. Balakin B, Hoffmann A, Kosinski P, Lee RD (2010). Eulerian-Eulerian CFD model for the sedimentation of spherical particles in suspension with high particle concentrations. *Engineering Applications of Computational Fluid Mechanics* 4(1):116-126.
2. Bitog JP, Lee IB, Shin MH, Hong SW, Hwang HS, Seo IH, Yoo JI, Kwon KS, Kim YH, Han JW (2009). Numerical simulation of an array of fences in Saemangeum reclaimed land. *Atmospheric Environment* 43(30):4612-4621.
3. Bourdin P, Wilson JD (2008). Windbreak aerodynamics: Is computational fluid dynamics reliable? *Boundary-Layer Meteorology* 126(2):181–208, DOI: 10.1007/ s10546-007-9229-y.
4. Bradley EF, Mulhearn PJ (1983). Development of velocity and shear stress distributions in the wake of a porous shelter fence. *Journal of Wind Engineering and Industrial Aerodynamics* 15(1–3):145–156, DOI: 10.1016/0167-6105(83)90185-X.
5. Cleugh HA (1998). Effects of windbreaks on airflow, microclimates and crop yields. *Agroforestry Systems* 41(1):55–84, DOI: 10.1023/A: 1006019805109.
6. FLUENT Inc. (2006). *FLUENT 6.3 User's Guide*. Lebanon, NH: FLUENT Inc.
7. Hinds WC (1999). *Aerosol Technology: Properties, Behavior and Measurement of Airborne Particles*. 2nd ed. New York: John Wiley &Sons, Inc.
8. Judd, MJ, Raupach MR, Finnigan JJ (1996). A wind tunnel study of turbulent flow around single and multiple windbreaks, part I: velocity fields. *Boundary-Layer Meteorology* 80:127–165.
9. Lin X (2006). *Simulation of Odor Dispersion Around Natural Windbreaks*. Ph.D. dissertation. McGill University, Ste-Anne-de-Bellevue, Quebec.
10. Melese Endalew A, Hertog M, Delele MA, Baetens K, Persoons T, Baelmans M, Ramon H, Nicolai BM, Verboven P (2009). CFD modeling and wind tunnel validation of airflow through plant canopies using 3D canopy architecture. *International Journal of Heat and Fluid Flow* 30(2):356-368.

11. Packwood AR (2000). Flow through porous fences in thick boundary layers: comparisons between laboratory and numerical experiments. *Journal of Wind Engineering and Industrial Aerodynamics* 88(1):75–90, DOI: 10.1016/S0167-6105(00)00025-8.
12. Petroff A, Mailliat A, Amielh M, Anselmet F (2008a). Aerosol dry deposition on vegetative canopies. Part I: Review of present knowledge. *Atmospheric Environment* 42(16):3625–3653, DOI: 10.1016/j.atmosenv.2007.09.043.
13. Petroff A, Mailliat A, Amielh M, Anselmet F (2008b). Aerosol dry deposition on vegetative canopies. Part II: A new modeling approach and applications. *Atmospheric Environment* 42(16):3654–3683, DOI:10.1016/j.atmosenv.2007.12.060.
14. Portela LM, Oliemans RVA (2006). Possibilities and limitations of computer simulations of industrial turbulent dispersed multiphase flows. *Flow, Turbulence and Combustion* 77(1–4):381–403, DOI: 10.1007/s10494-006-9051-5.
15. Purdy CW, Straus DC, Parker DB, Wilson SC, Clark RN (2004). Comparison of the type and number of microorganisms and concentration of endotoxin in the air of feedyards in the Southern High Plains. *American Journal of Veterinary Research* 65(1):45–52.
16. Raupach MR, Woods N, Dorr G, Leys JF, Cleugh HA (2001). The entrapment of particles by windbreaks. *Atmospheric Environment* 35(20):3373–3383, DOI: 10.1016/S1352-2310(01)00139-X.
17. Rogge WF, Medeiros PM, Simoneit BRT (2006). Organic marker compounds for surface soil and fugitive dust from open lot dairies and cattle feedlots. *Atmospheric Environment* 40(1):27–49, DOI: 10.1016/j.atmosenv.2005.07.076.
18. Rosenfeld M, Marom G, Bitan A (2010). Numerical simulation of the airflow across trees in a windbreak. *Boundary-Layer Meteorology* 135(1):89–107, DOI: 10.1007/s10546-009-9461-8.
19. Santiago JL, Martin F, Cuerva A, Bezdenejnykh N, Sanz-Andres A (2007). Experimental and numerical study of wind flow behind windbreaks. *Atmospheric Environment* 41(30):6406–6420, DOI: 10.1016/j.atmosenv.2007.01.014.
20. Tiwary A, Morvan HP, Colls JJ (2005). Modelling the size-dependent collection efficiency of hedgerows for ambient aerosols. *Journal of Aerosol Science* 37(8):990–1015, DOI: 10.1016/j.jaerosci.2005.07.004.
21. Tong XL, Luke EA (2010). Robust and accurate Eulerian multiphase simulations of icing collection efficiency using singularity diffusion model. *Engineering Applications of Computational Fluid Mechanics* 4(4):483-495.
22. Tu J, Yeoh GH, Liu C (2008). *Computational Fluid Dynamics: A Practical Approach*. Amsterdam: Butterworth-Heinemann.
23. Wang C, Lin Y (2006). Numerical simulation of three dimensional gas-particle flow in a spiral cyclone. *Journal of Applied Mathematics and Mechanics* 27(2):247–253, DOI: 10.1007/s10483-006-0214-1.
24. Wang H, Takle ES (1995). A numerical simulation of boundary-layer flows near shelterbelts. *Boundary-Layer Meteorology* 75(1-2):141–173, DOI: 10.1007/BF00721047.
25. Wilson JD (1985). Numerical studies of flow through a windbreak. *Journal of Wind Engineering and Industrial Aerodynamics* 21(2):119–154, DOI: 10.1016/0167-6105(85)90001-7.
26. Wilson JD, Yee E (2003). Calculation of wind disturbed by an array of fences. *Agricultural and Forest Meteorology* 115(1–2):31–50, DOI: 10.1016/S0168-1923(02)00169-7.
27. Zhang N, Zheng ZC, Maghirang RG (2008). Numerical simulation of smoke clearing with nanoparticle aggregates. *International Journal for Numerical Methods in Engineering* 74(4):601–618, DOI: 10.1002/nme.2186.